

Cite this: *Nanoscale*, 2020, **12**, 7651

# *In vivo* photothermal inhibition of methicillin-resistant *Staphylococcus aureus* infection by *in situ* templated formulation of pathogen-targeting phototheranostics†

Xujuan Guo,<sup>a</sup> Bing Cao,<sup>a</sup> Congyu Wang,<sup>a</sup> Siyu Lu <sup>b</sup> and Xianglong Hu <sup>\*a</sup>

Bacterial infection has caused a serious threat to human public health. Methicillin-resistant *Staphylococcus aureus* (MRSA) is a representative drug-resistant bacterium, which is difficult to eradicate completely, resulting in high infection probability with severe mortality. Herein, pathogen-targeting phototheranostic nanoparticles, Van-OA@PPy, are developed for efficient elimination of MRSA infection. Van-OA@PPy nanoparticles are fabricated from the *in situ* templated formation of polypyrrole (PPy) in the presence of ferric ions (Fe<sup>3+</sup>) and a polymer template, hydrophilic poly(2-hydroxyethyl methacrylate-co-N,N-dimethyl acrylamide), P(HEMA-co-DMA). PPy nanoparticles are further coated with vancomycin conjugated oleic acid (Van-OA) to afford the resultant pathogen-targeting Van-OA@PPy. A high photothermal conversion efficiency of ~49.4% is achieved. MRSA can be efficiently killed due to sufficient nanoparticle adhesion and fusion with MRSA, followed by photothermal therapy upon irradiation with an 808 nm laser. Remarkable membrane damage of MRSA is observed, which contributes greatly to the inhibition of MRSA infection. Furthermore, the nanoparticles have high stability and good biocompatibility without causing any detectable side effects. On the other hand, residual Fe<sup>3+</sup> and PPy moieties in Van-OA@PPy endow the nanoparticles with magnetic resonance (MR) imaging and photoacoustic (PA) imaging potency, respectively. The current strategy has the potential to inspire further advances in precise diagnosis and efficient elimination of MRSA infection in biomedicine.

Received 7th January 2020,

Accepted 7th March 2020

DOI: 10.1039/d0nr00181c

rsc.li/nanoscale

## 1. Introduction

Pathogenic bacteria have been widely threatening human beings for a long time.<sup>1,2</sup> Since the introduction of commercial penicillin in the 1950s, antibiotics have become an important weapon to combat pathogenic microorganisms.<sup>3,4</sup> Antibiotics can effectively inhibit bacteria *via* diverse pathways, such as inhibition of cell wall synthesis, protein synthesis or DNA replication. In the past few decades, the optimistic situation has been tempered by the emergence of bacteria with resistance to antibiotics.<sup>5–8</sup> One serious so-called “hospital superbug”, methicillin-resistant *Staphylococcus aureus* (MRSA), which is resistant to almost all existing  $\beta$ -lactam antibiotics, has resulted in more and more intractable infections such as

subcutaneous abscesses, endocarditis, septic arthritis, and even some acute fatal events.<sup>9,10</sup> A key feature of MRSA infection is recurrence.<sup>11–13</sup> Recurrent infections usually require repeated antibiotic treatments that would result in serious multi-drug resistance.<sup>14,15</sup> Subcutaneous abscesses can be treated clinically by incision and drainage, which is painful and can definitely increase the risk of additional infection.<sup>16</sup>

Some effective antimicrobial methods have been proposed to inhibit pathogen infection, such as amphiphilic polymers,<sup>17–19</sup> antimicrobial peptides (AMPs),<sup>20–22</sup> photodynamic therapy (PDT),<sup>23–26</sup> and other smart therapeutic systems.<sup>27–32</sup> Compared with conventional small molecule antibiotics, polymeric antimicrobials can cause physical damage to the microbial cell membrane, thereby reducing the possibility of drug resistance developing.<sup>17</sup> Furthermore, photothermal therapy (PTT), using photothermal agents to convert light energy into heat, can destroy bacteria *via* thermal damage to the cell wall and denaturation of proteins/enzymes. Recently, PTT has been increasingly utilized as a popular non-invasive and localized treatment modality.<sup>23,33–36</sup> In addition, NIR light with outstanding deep tissue penetration is suitable for *in vivo* PTT treatment.<sup>37,38</sup> Some nanomaterials have been

<sup>a</sup>MOE Key Laboratory of Laser Life Science & Institute of Laser Life Science, College of Biophotonics, South China Normal University, Guangzhou, 510631, China.

E-mail: xlhu@sncu.edu.cn, huxlong@mail.ustc.edu.cn

<sup>b</sup>Green Catalysis Center, and College of Chemistry, Zhengzhou University, Zhengzhou, 450000, China

†Electronic supplementary information (ESI) available. See DOI: 10.1039/d0nr00181c

developed to achieve efficient photothermal sterilization for bacteria eradication.<sup>20,39,40</sup> Nevertheless, tedious multistep synthesis or formulation procedures for the nanomaterials frequently limit their further applications. Polypyrrole (PPy) has been applied for cancer theranostic applications due to its excellent *in vitro* and *in vivo* biocompatibility, facile fabrication, significant photothermal conversion, and remarkable photostability.<sup>41–45</sup> However, the exploration of PPy for pathogen imaging and inhibition is still in its infancy.<sup>46</sup>

Furthermore, another challenging issue is antibacterial selectivity towards bacteria over human cells in infected tissues, which has restricted their success in clinical applications.<sup>17,47,48</sup> Non-specific heat potentially causes huge damage to healthy tissues. If photothermal agents or nanomaterials can image the infected area and selectively adhere to pathogens,<sup>41</sup> then the following photothermal treatment could potentially achieve highly efficient precise therapy with reduced side effects. In addition, it is critically important to develop a photothermal agent that can serve as a contrast agent for simultaneous imaging *in vivo*. Therefore, it is extremely important and urgent to develop facilely formulated photothermal materials to integrate pathogen targeting, real-time imaging, and precise treatment simultaneously.<sup>49</sup> In addition, vancomycin is a glycopeptide antibiotic with high affinity to the terminal peptide (D-alanyl-D-alanine) on the cell wall of MRSA,<sup>50–52</sup> and thus it is a potential targeting ligand for MRSA.

Herein, pathogen-targeting PPy nanoparticles, Van-OA@PPy, were formulated *via in situ* templated formulation and further co-assembly with vancomycin conjugated oleic acid (Van-OA), and exhibited efficient photothermal transformation and precise theranostic applications for MRSA elimination. Furthermore, residual Fe<sup>3+</sup> and the PPy moieties endow the Van-OA@PPy nanoparticles with persistent magnetic resonance (MR) imaging and photoacoustic (PA) imaging potency for infected lesion sites.

## 2. Experimental

### 2.1 Materials

Pyrrole (98%, Aldrich), oleic acid (OA, Aldrich), *N,N*-dimethyl acrylamide (DMA, 98%, Merck), 2-hydroxyethyl methacrylate (HEMA, 99.5%, J&K), 1-(3-dimethylaminopropyl)-3-ethylcarbodiimide hydrochloride (EDC, Merck), *N*-hydroxysuccinimide (NHS, Merck), and vancomycin hydrochloride (Van-HCl, 98%, Aladdin) were used as received without further purification. SYTO 9 and propidium iodide (Invitrogen LIVE/DEAD BacLight bacterial viability kit, L7012) were purchased from Thermo Fisher Scientific Company. Dimethylformamide (DMF), dimethylsulfoxide (DMSO), chloroform (CHCl<sub>3</sub>), 1,4-dioxane and all other organic solvents were available from the Guangzhou Chemical Reagent Company. Water was deionized with a Milli-QSP reagent water system (Millipore) to a specific resistivity of 18.4 MΩ cm. 4-Cyanopentanoic acid dithiobenzoate (CPADB) was synthesized as reported previously.<sup>53,54</sup>

### 2.2 Sample preparation

The synthetic routes employed for the preparation of Van-OA@PPy NPs are shown in Fig. S1† and Fig. 1.

**2.2.1 Synthesis of P(HEMA-*co*-DMA).** The reversible addition fragmentation chain transfer (RAFT) polymerization technique was employed to synthesize hydrophilic P(HEMA-*co*-DMA).<sup>45</sup> Typically, CPADB (21 mg, 0.075 mmol), HEMA (1476 mg, 11.34 mmol), DMA (1125 mg, 11.34 mmol), and AIBN (2.5 mg, 0.015 mmol) were added into a glass ampoule containing 4 mL 1,4-dioxane. The ampoule was then degassed *via* three freeze-pump-thaw cycles and flame-sealed under vacuum. The ampoule was then immersed into an oil bath at 70 °C to start the polymerization. After 12 h, the ampoule was quenched in liquid nitrogen to terminate the polymerization. The mixture was precipitated into an excess of diethyl ether to generate pale residues, and the residues were dissolved in dichloromethane and precipitated into diethyl ether, which was repeated three times. The product was dried in a vacuum oven overnight at room temperature. The degree of polymerization (DP) of HEMA and DMA was determined to be 220 and 188, respectively (Fig. S2†).

**2.2.2 Synthesis of Van-OA.** Oleic acid (OA, 31 mg, 0.11 mmol) was activated in the presence of EDC (22.2 mg, 0.12 mmol) and NHS (12 mg, 0.12 mmol) in anhydrous DMSO and CHCl<sub>3</sub> (1 : 1, 2 mL) in a glass ampoule. After stirring for 10 h at room temperature, the solution was mixed with Van-HCl (163.4 mg, 0.11 mmol) in anhydrous DMSO.<sup>55</sup> After stirring at room temperature for 12 h, the reaction mixture was dialyzed against deionized water, and then lyophilized as a pale solid to afford the resultant Van-OA (Fig. S3†).

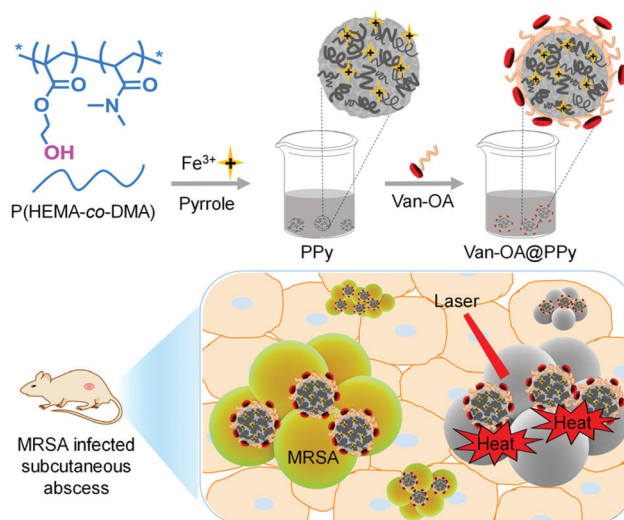


**Fig. 1** Schematic illustration for *in situ* formulation of pathogen-targeting phototheranostic nanoparticles, Van-OA@PPy, for photothermal inhibition of MRSA infection. P(HEMA-*co*-DMA) was employed as a template to afford polypyrrole (PPy) *in situ* in the presence of Fe<sup>3+</sup>, and then PPy was further self-assembled with vancomycin-tethered oleic acid (Van-OA) to afford the resultant phototheranostic Van-OA@PPy.

**2.2.3 *In situ* templated formulation of Van-OA@PPy.** Stable PPy nanoparticles were prepared in the presence of a polymer template, P(HEMA-*co*-DMA).<sup>45,56</sup> Briefly, 60 mg P(HEMA-*co*-DMA) was dissolved in 15 mL DI water at room temperature, and then FeCl<sub>3</sub>·6H<sub>2</sub>O (43.5 mg, 0.16 mmol) was added to the solution. After stirring for 30 min, pyrrole (50 μL, 0.72 mmol) was added to the mixture to initiate polymerization. After reacting for 24 h, the resultant black PPy dispersion was afforded by dialysis against deionized water for 2 h. After that, Van-OA (2.0 mg, 1.14 μM) was dissolved in DMSO and CHCl<sub>3</sub> (1 : 1, v/v), and then added dropwise to the PPy aqueous dispersion with vigorous stirring. The resultant Van-OA@PPy nanoparticles were finally formulated after dialysis and repeated centrifugation to remove unreacted species.

### 2.3 Characterization

The hydrodynamic diameter distribution and ζ potential were determined using a Malvern Zetasizer Nano ZS90 instrument (Malvern, UK). Transmission electron microscopy (TEM) analysis was performed on a JEOL JEM-2100. Scanning electron microscopy (SEM) analysis was performed on a Hitachi S-3000N. The UV-visible-NIR extinction spectra of the nanoparticles were analyzed by a UV-visible spectrophotometer (Lambda 35, PerkinElmer, USA). MR relaxivities were measured using a 1 T MR scanner (NM-G1, Shanghai Niumag Co., China). For photothermal evaluation, a MikroShot thermal camera (Mikron) was used to collect thermal images and quantify the temperature of the aqueous dispersions. Photoacoustic (PA) imaging was performed on a home-made system with a 10 MHz 384-element ring ultrasound array at 10 mJ cm<sup>-2</sup>, and an optical parametric oscillator (OPO) (Surelite II-20, Continuum, Santa Clara, CA, USA) with 4–6 ns pulse duration and 20 Hz pulse repetition rate as the light source.

### 2.4 Bacteria culture

A single colony of MRSA on a solid Mueller–Hinton (MH) agar plate was transferred to 10 mL of MH liquid culture medium and cultured at 37 °C overnight. The bacteria were then harvested by centrifuging at 6000 rpm for 3 min and washed with PBS three times. The bacteria pellet was then resuspended in PBS and diluted to the desired density based on OD<sub>600</sub> = 0.1.

### 2.5 Minimum bactericidal concentration (MBC) measurements

The MBCs of the nanoparticles were determined by the broth microdilution method.<sup>57</sup> Briefly, a series of 2-fold dilution dispersions of Van-OA@PPy, PPy (2000, 1000, 500, 250, 125, 63 μg mL<sup>-1</sup>) and Van-OA (at an equivalent dosage gradient to Van-OA@PPy) were prepared and added to an equal volume of bacterial solution (0.1 mL) containing approximately 1 × 10<sup>6</sup> CFU mL<sup>-1</sup> in each well of a 96-well plate and incubated for 30 min. The mixture was subjected to NIR irradiation (808 nm, 1.0 W cm<sup>-2</sup>) for 5 min. Then, the resultant bacterial suspensions were cultured in LB agar medium at 37 °C overnight. The bacteria colonies were counted. The MBC values were determined

as the lowest concentrations of nanoparticles that reduced the viability of the initial bacterial inoculum by ≥99.9%. Growth medium containing only microbial cells was used as the negative control. Each MBC test was carried out in 3 replicates and repeated 3 times.

### 2.6 Membrane potential analysis

In order to verify whether the antimicrobial nanomaterial can depolarize the bacterial membrane potential, a BacLight bacterial membrane potential kit is used in this study.<sup>24</sup> The cytometer evaluates the change in bacterial membrane potential. It is known that DiOC<sub>2</sub>(3) exhibits red fluorescence in bacterial cells with intact membranes, and when the fluorescence shifts to green, it indicates depolarization of the membrane potential. MRSA cells were inoculated in the mid-log phase. Viable cells were then diluted to 2.5 × 10<sup>7</sup> CFU mL<sup>-1</sup> in PBS and added to various samples with the indicated contents. For the light-treatment groups, an 808 nm laser was employed at 1.0 W cm<sup>-2</sup>, and light irradiation continued for 5 min. After various treatments for 30 min at 37 °C, DiOC<sub>2</sub>(3) was added to the samples at 30 μM and further incubated for 30 min. Membrane potential analysis was carried out using a flow cytometer to determine the ratio of cells that exhibited red fluorescence to those that displayed green fluorescence. Gates were determined based on the untreated control. Data were representative of two independent assays repeated in duplicate.

### 2.7 Transmittance electron microscopy (TEM) and scanning electron microscopy (SEM) analysis

MRSA dispersions (10<sup>8</sup> CFU mL<sup>-1</sup>, 0.1 mL) were incubated with aqueous dispersions of Van-OA@PPy, PPy, and Van-OA. After light irradiation for 5 min (808 nm, 1.0 W cm<sup>-2</sup>), one drop of the dispersion was placed on a formvar/carbon coated 200 mesh copper grid and dried at room temperature. TEM analysis was performed under a JEM-2100 transmittance electron microscope (JEOL, Japan). For SEM analysis, after various treatments, the MRSA dispersions were washed three times with PBS and then fixed with 2.5% glutaraldehyde for 4 h. After fixation, the samples were washed three times with PBS and dehydrated in a series of alcohol solutions. Finally, the samples were dispersed by metal spraying and observed by SEM.

### 2.8 *In vitro* evaluation of cytotoxicity and biocompatibility

MTT assays were carried out to evaluate the cytotoxicity of antimicrobial polymer nanoparticles towards normal cells under light. RAW 264.7 cells were seeded onto 96-well plates (5 × 10<sup>3</sup> cells per well). Following cultivation for 12 h, different concentrations of Van-OA@PPy were added into the wells and incubated in the dark for 24 h. MTT solution (20 μL, 5 mg mL<sup>-1</sup>) was added into each well. After incubation for 4 h at 37 °C, the MTT solution was replaced with DMSO in each well. The absorbance was determined at 530 nm using a microplate reader (Infinite M200, TECAN).

## 2.9 Hemolysis assays

The hemolytic behavior of the nanoparticles was tested using mouse red blood cells (RBCs). Firstly, 1 mL of blood sample was added to 2 mL of 0.9% NaCl solution, and then RBCs were isolated from the serum by centrifugation at 1000 rpm for 10 min. After washing three times with 5 mL of 0.9% NaCl solution, 50  $\mu\text{L}$  of RBC suspension in 0.9% NaCl solution was placed in each well of a 96-well plate and 50  $\mu\text{L}$  of Van-OA@PPy at different concentrations (1000, 500, 250, 125, 63  $\mu\text{g mL}^{-1}$ ) was added to each well. The plates were incubated for 3 hours at 37  $^{\circ}\text{C}$ , and then the cell suspensions were taken out and centrifuged at 1000 rpm for 5 min. Aliquots (50  $\mu\text{L}$ ) of the supernatant were transferred to 96-well plates, and the corresponding hemoglobin release was monitored at 576 nm using a microplate reader. The RBC suspension in 0.9% NaCl solution was used as a negative control, and the absorbance of RBCs lysed by pure water was taken as 100% hemolysis.

## 2.10 *In vivo* cytotoxicity assays

An aqueous dispersion of Van-OA@PPy was intravenously injected into female Balb/c mice. At 24 h post-injection, the mice were sacrificed, and hematological and blood biochemical analyses were performed.

## 2.11 *In vivo* inhibition and imaging of MRSA infection

All animal procedures were performed following the Guidelines for Care and Use of Laboratory Animals of South China Normal University and approved by the Animal Ethics Committee of South China Normal University. Female Balb/c mice aged 6–7 weeks were purchased from the Experimental Animal Center of Southern Medical University. To evaluate the therapeutic efficacy of Van-OA@PPy for bacterial infection, a subcutaneous abscess was experimentally created in each test mouse. MRSA ( $10^9$  CFU) in PBS solution (0.1 mL) was injected into the shaved backs of the mice. At 24 h post-injection, an infected swelling formed in each test mouse. The infected mice were randomly assigned to seven groups ( $n = 6$ ): (1) control (only injected with PBS); (2) PBS + 808 nm laser irradiation; (3) PPy injection alone; (4) Van-OA injection alone; (5) Van-OA@PPy injection alone; (6) PPy injection + 808 nm laser irradiation; (7) Van-OA@PPy injection + 808 nm laser irradiation. The sample dispersions were directly injected into the infected sites. Light irradiation was performed for 5 min at 0.5  $\text{W cm}^{-2}$  in each treatment. On the seventh day of treatment, mice were randomly sacrificed in each group, and the affected tissues were collected for tissue homogenization. The number of bacteria in each mouse wound was evaluated by the agar plate dilution method. The mice were finally euthanized, and the infected wounds were harvested for histology analysis by hematoxylin and eosin staining (H&E staining).

## 2.12 *In vivo* MR/PA imaging

A dispersion of Van-OA@PPy was directly injected into the infected sites of female Balb/c mice with subcutaneous abscesses, and the mice were imaged and analyzed before injection and

post-injection after 12 h, 24 h, and 48 h. *In vivo* MR imaging was performed accordingly. On the other hand, PA imaging of the infected sites was performed over the same time duration.

# 3. Results and discussion

## 3.1 Fabrication and characterization of pathogen-targeting photothermal nanoparticles

First of all, the formulation and characterization of the photothermal nanoparticles are described. Hydrophilic P(HEMA-*co*-DMA) was employed as a polymer template to generate PPy *in situ*. Reversible addition fragmentation chain transfer (RAFT) polymerization was employed to polymerize 2-hydroxyethyl methacrylate (HEMA) and *N,N*-dimethyl acrylamide (DMA) to afford hydrophilic P(HEMA-*co*-DMA) (Fig. S1(a) in the ESI†). The activation of oleic acid (OA) by NHS/EDC, followed by conjugation with vancomycin could afford Van-OA (Fig. S1(b)†). The corresponding products were characterized by  $^1\text{H}$  NMR and FT-IR analysis (Fig. S2 and S3†). Narrowly dispersed PPy nanoparticles were fabricated *via* facile one-step aqueous polymerization in water.<sup>45,56</sup> Then, the mean hydrodynamic diameters of PPy and Van-OA@PPy aqueous dispersions were determined by dynamic light scattering (DLS) to be  $\sim 75$  nm and  $\sim 90$  nm, respectively (Fig. 2(a)). TEM analysis also

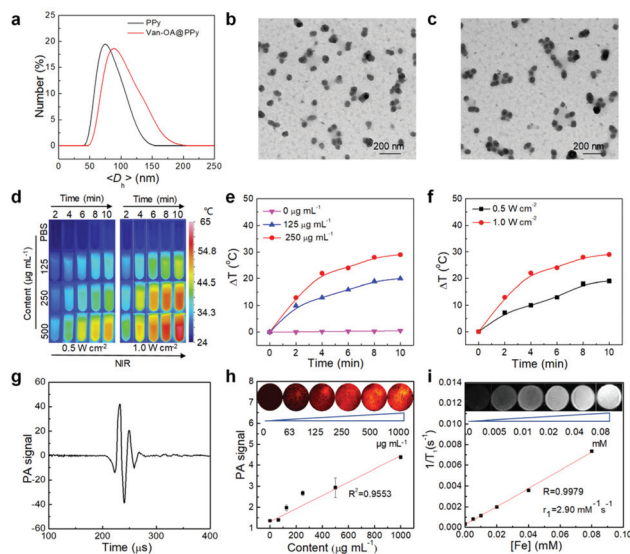


**Fig. 2** Physicochemical characterization of blank PPy and Van-OA@PPy. (a) Hydrodynamic diameter distributions recorded for PPy and Van-OA@PPy NPs. TEM images of (b) PPy and (c) Van-OA@PPy. (d) Thermographic images of Van-OA@PPy upon laser treatment. (e) Temperature elevation of Van-OA@PPy with various concentrations upon 10 min exposure to an 808 nm laser at 1.0  $\text{W cm}^{-2}$ . (f) Temperature elevation of Van-OA@PPy (250  $\mu\text{g mL}^{-1}$ ) upon 10 min exposure to 808 nm laser light with different power densities (0.5, 1.0  $\text{W cm}^{-2}$ ). (g) Photoacoustic (PA) amplitudes of Van-OA@PPy upon irradiation with a pulsed 808 nm laser. (h) PA signals of Van-OA@PPy with different concentrations at 808 nm (inset: *in vitro* PA images). (i) Plot of  $1/T_1$  against  $\text{Fe}^{3+}$  content and corresponding  $T_1$  weighted MR images (inset) recorded for Van-OA@PPy.

confirmed fine mono-dispersity for both PPy and Van-OA@PPy, exhibiting diameters of less than 50 nm (Fig. 2(b) and (c)). Furthermore, the dispersions of PPy and Van-OA@PPy with black color both had broad absorption in the NIR range (Fig. S4†). In addition, both PPy and Van-OA@PPy NPs were positively charged by over 20 mV, which was favorable for adhering to negatively charged bacteria (Fig. S5†).

### 3.2 Photothermal/photoacoustic effect

Upon light irradiation by an 808 nm continuous laser, the temperature change of the nanoparticle dispersion was measured. Van-OA@PPy showed a rapid and continuous temperature increase within 10 min (Fig. 2(d)). The rate of temperature increase was positively correlated with the nanoparticle content, laser power density, and irradiation time (Fig. 2(e) and (f)). The temperature increase of Van-OA@PPy could be as high as 29 °C, which was much higher than that of water (<3 °C), which implied good photothermal ability. Notably, the temperature range could be modulated by the nanoparticle contents, laser power and irradiation time to meet practical requirements and avoid potential side effects resulting from hyperthermia. These results confirmed that Van-OA@PPy could efficiently convert light energy into heat.

After that, the photothermal conversion efficiency ( $\eta$ ) was examined to visually evaluate the photothermal conversion properties of Van-OA@PPy. The parameter was measured by a method similar to previous reports.<sup>58,59</sup> The temperature change of a Van-OA@PPy aqueous dispersion was recorded as a function of time under continuous irradiation by an 808 nm laser until a steady state temperature was reached (Fig. S6(a) and (b)†). These results showed that the aqueous dispersion of Van-OA@PPy exhibited the highest temperature elevation upon continuous irradiation for ~360 s, and its temperature remained constant as the time increased further. Subsequently, the irradiation was shut off, and the temperature decrease of the aqueous dispersion was monitored to determine the rate of heat transfer from the dispersion system to the environment. The detailed calculation is as follows:

$$\eta = \frac{hS\Delta T_{\max} - Q_s}{I(1 - 10^{-A_{808}})} \quad (1)$$

where  $\Delta T_{\max}$  is the temperature change of the nanoparticle suspensions at the maximum steady-state temperature,  $Q_s$  expresses the heat associated with the NIR light absorbance of the solvent,  $I$  is the incident laser power ( $1.5 \text{ W cm}^{-2}$ ), and  $A_{808}$  (1.8210) is the absorbance of Van-OA@PPy at 808 nm.  $h$  is the heat transfer coefficient, and  $S$  is the surface area of the container. The value of  $hS$  is derived according to eqn (2):

$$\tau = \frac{m_s c_s}{hS} \quad (2)$$

where  $\tau$  is the sample system time constant, and  $m_s$  and  $c_s$  are the mass and the heat capacity of the solvent (pure water), respectively. Thus, the 808 nm laser heat conversion efficiency ( $\eta$ ) of Van-OA@PPy can be calculated to be 49.4%. This value is higher than those reported for gold nanoshells (13%), gold

nanorods (22%), and iron oxide nanoparticles (43%).<sup>60,61</sup> Herein, the high photothermal conversion efficacy made it a good candidate for an efficient photothermal agent. Furthermore, the photostability of Van-OA@PPy was evaluated by irradiating the dispersion with the 808 nm laser at a high power density of  $2 \text{ W cm}^{-2}$ , and then cooling to room temperature. After four cycles of testing, the extent of temperature increase varied minimally, which indicated the high photostability of Van-OA@PPy due to the native stability of PPy (Fig. S7†).<sup>45</sup>

On the other hand, because of its good photothermal ability, the photoacoustic (PA) properties of Van-OA@PPy were examined for potential imaging applications. The PA amplitudes of Van-OA@PPy were observed distinctly on exposure to an 808 nm pulsed laser at a power density of  $0.3 \text{ W cm}^{-2}$  (Fig. 2(g)), and the signals were enhanced linearly with increasing concentration, which was beneficial for further PA imaging (Fig. 2(h)).

### 3.3 MRI relaxation properties

Due to the residual Fe element in the resultant Van-OA@PPy nanoparticles,<sup>35,62</sup> the MR imaging capability of Van-OA@PPy was investigated. The  $T_1$  relaxivity ( $r_1$ ) for aqueous dispersions of Van-OA@PPy was obtained by measuring  $T_1$  for various  $\text{Fe}^{3+}$  contents (Fig. 2(i)). The  $r_1$  value of Van-OA@PPy was calculated from the slope of this plot to be  $2.90 \text{ mM}^{-1} \text{ s}^{-1}$ . The corresponding *in vitro*  $T_1$ -weighted MR images of Van-OA@PPy with different  $\text{Fe}^{3+}$  contents were also recorded, indicating enhanced brightness on increasing the Fe content from 0 to 0.08 mM (Fig. 2(i) inset).

### 3.4 In vitro MRSA inhibition

Based on the standard broth microdilution method, an *in vitro* bacterial inhibition was performed for MRSA.<sup>63</sup> The colony formation unit (CFU) values of each group were observed to decrease with increasing concentrations of PPy and Van-OA@PPy (Fig. 3). As shown in Fig. 3(a), representative plates of the Van-OA@PPy + NIR group had no bacteria, which confirmed the remarkable MRSA killing potency. Notably, PPy and Van-OA@PPy displayed obvious antibacterial activity in a dose-dependent manner. The cell viabilities of MRSA without NIR

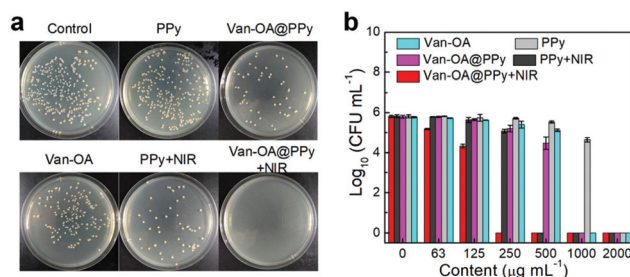


Fig. 3 Antibacterial activity towards MRSA for various samples. (a) Bacterial colony formation of MRSA treated with different samples and (b) the related quantitative results.

irradiation were obviously reduced when the concentrations of PPy and Van-OA@PPy were higher than  $1000 \mu\text{g mL}^{-1}$ . In contrast, the viability of the bacteria dramatically decreased to 0% at a dose of  $250 \mu\text{g mL}^{-1}$  upon NIR irradiation for 10 min (Fig. 3(b)). Both PPy and Van-OA@PPy exhibited good antibacterial ability against MRSA due to the main contribution being *via* photothermal damage.

The antibacterial mechanism of pathogen-targeting Van-OA@PPy was also examined in due course. To determine whether Van-OA@PPy could depolarize the bacterial cell membrane, the dynamic change in the bacterial membrane potential was monitored by flow cytometry using a bacterial membrane potential kit. The carbocyanine dye DiOC<sub>2</sub>(3) emits green fluorescence in all bacteria, but the fluorescence is red-shifted at higher cytosolic concentrations because of the larger membrane potentials. The ratio of red and green fluorescence was employed to evaluate the membrane potential. A flow cytometry gate (black polygon) was drawn to indicate the normal bacteria (Fig. 4(a)). Compared to the other groups, the Van-OA@PPy treated bacteria exhibited enhanced green fluorescence and reduced red fluorescence under light irradiation. Furthermore, the red/green fluorescence ratio was quantitatively determined (Fig. 4(b)). The Van-OA@PPy + NIR group exhibited the lowest red/green ratio compared with the other groups, which demonstrated that the photothermal effect could lead to the most significant membrane damage. Thus, the flow cytometry assays further confirmed that Van-OA@PPy could depolarize the membrane of MRSA.

After that, the morphological changes of MRSA after various treatments were further observed by transmission electron microscopy (TEM) and scanning electron microscopy (SEM) (Fig. 4(c) and (d)). MRSA cells in the control group had

intact and smooth cell membranes. When the bacterial cells were incubated with PPy and Van-OA@PPy, many nanoparticles were observed to adhere to the bacterial surface. Whereas for the Van-OA@PPy + NIR group, sunken cell membranes and even total disruption were observed. These remarkable morphology changes showed that the photothermal effect of Van-OA@PPy could effectively disrupt the bacterial membrane, thus promoting the efficient elimination of MRSA.

### 3.5 Biocompatibility evaluation

Van-OA@PPy could be employed as a phototheranostic agent in biomedicine, thus MTT assays using RAW 264.7 cells were performed to determine the cell viabilities upon incubation with nanoparticles. Encouragingly, the cytotoxicity of Van-OA@PPy was minimal even up to a high concentration of  $1000 \mu\text{g mL}^{-1}$ , suggesting remarkable biocompatibility (Fig. 5(a)). Furthermore, the hemolytic activity of Van-OA@PPy

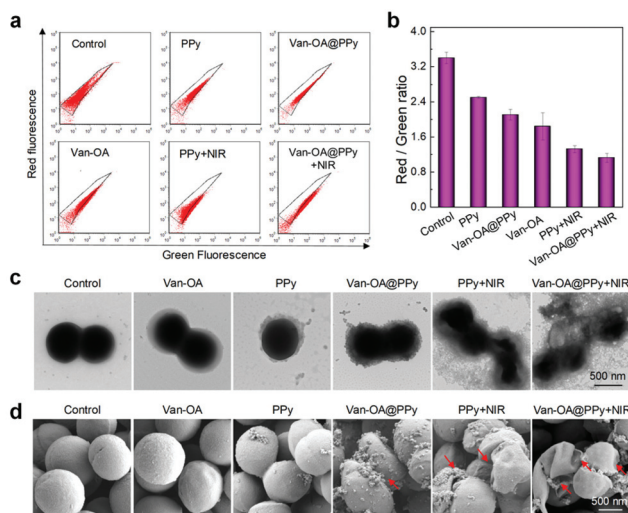


**Fig. 4** *In vitro* MRSA inhibition and membrane damage evaluation in MRSA. (a) Membrane potential flow cytometric dot plots obtained for MRSA after incubating with  $30 \mu\text{M}$  DiOC<sub>2</sub>(3) for 30 min by flow cytometry using a bacterial membrane potential kit. (b) Red/green fluorescence ratios calculated from (a). Morphological changes of MRSA after various treatments observed by (c) TEM and (d) SEM.

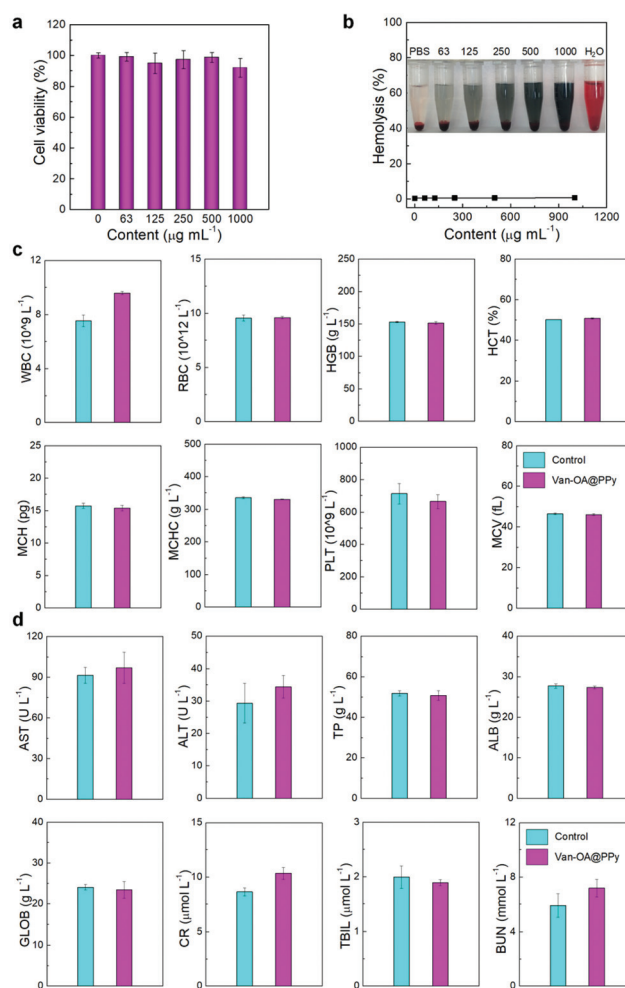


**Fig. 5** Biocompatibility evaluation for pathogen-targeting phototheranostic Van-OA@PPy. (a) Cell viability of Van-OA@PPy towards RAW 264.7 cells determined by an MTT assay. (b) Hemolysis quantification of mouse red blood cells upon treatment with Van-OA@PPy at various concentrations. (c) Hematological data and (d) blood biochemical analysis for mice 24 h post-injection with Van-OA@PPy.

towards mouse red blood cells was evaluated.<sup>64</sup> Van-OA@PPy displayed no observable hemolytic effect even at  $1000 \mu\text{g mL}^{-1}$  (Fig. 5(b)). Finally, blood biochemical analyses were conducted in mice 24 h post-injection with Van-OA@PPy. There were no significant changes in the hematological data and blood biochemicals compared with the normal group (Fig. 5(c) and (d)). Herein, Van-OA@PPy had good blood safety during blood circulation. In summary, Van-OA@PPy had low *in vitro* toxicity and high blood biocompatibility, thus it was safe to use as a phototheranostic agent for *in vivo* applications.

### 3.6 *In vivo* MR/PA imaging of MRSA infection

An MRSA-infected mouse subcutaneous abscess model was fabricated to evaluate the PTT efficacy of Van-OA@PPy. The retention of Van-OA@PPy was reflected by the MR and PA signals at the infection site. At 48 h post-injection, the MR signal was observed to be  $\sim 1.29$ -fold higher in comparison to the untreated control (Fig. 6(a) and (b)).<sup>65</sup> PA imaging of the infection site further confirmed the extended retention of Van-OA@PPy at the infection site (Fig. S8†). Long retention of Van-OA@PPy is beneficial in reducing the frequency of drug administration and also extending the duration of real-time imaging.

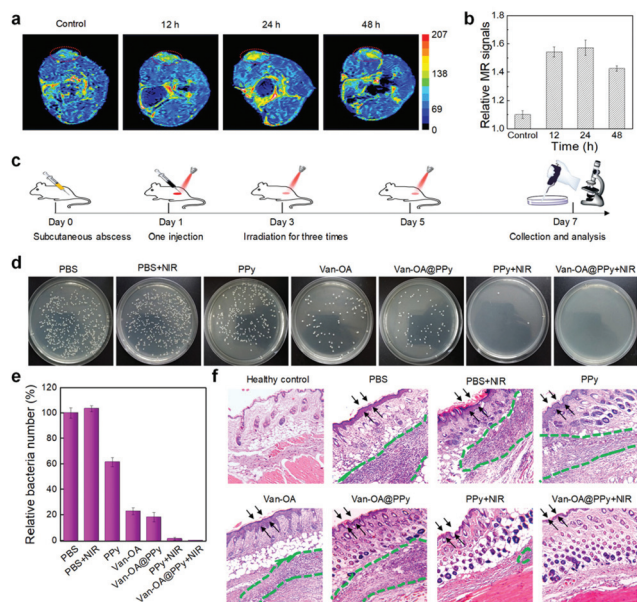


**Fig. 6** *In vivo* MR imaging and treatment of MRSA-infected subcutaneous abscesses. (a) *In vivo*  $T_1$ -weighted MR images of a mouse before and after injection of Van-OA@PPy (red circles indicate subcutaneous abscess sites). (b) Relative MR signals of the infected abscess sites. (c) Schematic illustration of the treatment process of the mouse subcutaneous abscess model. (d) Digital images of bacteria colonies from the MRSA-infected subcutaneous abscesses at day 7. (e) Relative bacteria numbers of the subcutaneous abscesses at day 7. (f) Histologic analysis of the wound tissue after various treatments by hematoxylin and eosin (H&E) staining (dotted lines indicate inflammatory cell aggregates on the infected skin, and the arrows indicate the epidermis). Skin tissue from uninfected mice served as a healthy control.

### 3.7 *In vivo* therapeutic efficacy

Finally, the *in vivo* inhibition efficacy was assessed against MRSA infected mouse subcutaneous abscesses. Seven groups were examined in our parallel experiments, and a PBS injection was used as a control (Fig. 6(c)). Only one injection was given in the therapeutic process. At the 7th day, the mice were sacrificed, and the relevant abscess tissues were harvested, separated, and homogenized for further evaluation. The bacteria burden in each mouse was evaluated by the agar plate dilution method during the treatment process (Fig. 6(d) and (e)). MRSA was significantly inhibited in the Van-OA@PPy + NIR group, whereas bacteria still survived in the other groups. Furthermore, histological analysis of the infected area was performed for each treatment (Fig. 6(f)). The untreated PBS group had a large number of inflammatory cells (indicated by green dotted lines), no intact hair follicles, and thickened epidermis. By contrast, the healed epithelial tissue in the Van-OA@PPy + NIR group was filled with many hair follicles and the epidermal thickness was quite comparable with that of the healthy control, while the epidermis in the other groups was much thicker than in the healthy control, suggesting a limited extent of recovery in these groups. Thus, Van-OA@PPy + NIR could precisely sterilize *in vivo* MRSA infection in mouse subcutaneous abscesses, suggesting outstanding photothermal inhibition capability for MRSA infection. The local temperature variation of an MRSA infected mouse was monitored by an infrared thermal camera (Fig. S9†). Upon *in situ* treatment and laser irradiation, the temperature of the abscess area after injection with Van-OA@PPy and PPy was much higher than that of the PBS group, but lower than  $45^\circ\text{C}$ . Furthermore, the tissue around the abscess didn't exhibit significant heat conduction, thus avoiding thermal damage to peripheral healthy tissues.

## 4. Conclusions

In conclusion, *in situ* formulated pathogen-targeting Van-OA@PPy nanoparticles were developed to achieve precise photothermal eradication of MRSA infection, which was imaged by dual-modality MR and PA imaging. Van-OA@PPy could efficiently convert light energy into local heat with an extremely high photothermal conversion efficiency, which was determined to be  $\sim 49.4\%$ . Furthermore, the phototheranostic platform was biocompatible without any detectable side effects. This strategy has provided an effective candidate for the treatment of MRSA infection, and paved a solid foundation for precise phototheranostics of pathogens in clinical medicine.

## Conflicts of interest

There are no conflicts to declare.

## Acknowledgements

This work was supported by the National Natural Scientific Foundation of China (51973071, 21674040), the Natural Science Foundation for Distinguished Young Scholars of Guangdong Province (2016A030306013), the Pearl River Young Talents Program of Science and Technology in Guangzhou (201906010047), the Scientific Research Projects of Guangzhou (201805010002), and the National Key Research and Development Program of China (2018YFA0209800).

## References

- 1 K. E. Jones, N. G. Patel, M. A. Levy, A. Storeygard, D. Balk, J. L. Gittleman and P. Daszak, *Nature*, 2008, **451**, 990–994.
- 2 X. Li, H. T. Bai, Y. C. Yang, J. Yoon, S. Wang and X. Zhang, *Adv. Mater.*, 2019, **31**, 1805092.
- 3 J. Davies, *Science*, 1994, **264**, 375–382.
- 4 Y. M. Li, G. H. Liu, X. R. Wang, J. M. Hu and S. Y. Liu, *Angew. Chem., Int. Ed.*, 2016, **55**, 1760–1764.
- 5 M. N. Alekshun and S. B. Levy, *Cell*, 2007, **128**, 1037–1050.
- 6 V. M. D'Costa, K. M. McGrann, D. W. Hughes and G. D. Wright, *Science*, 2006, **311**, 374–377.
- 7 S. B. Levy and B. Marshall, *Nat. Med.*, 2004, **10**, S122–S129.
- 8 M. F. Richter, B. S. Drown, A. P. Riley, A. Garcia, T. Shirai, R. L. Svec and P. J. Hergenrother, *Nature*, 2017, **545**, 299–304.
- 9 T. Jin, M. Bokarewa, T. Foster, J. Mitchell, J. Higgins and A. Tarkowski, *J. Immunol.*, 2004, **172**, 1169–1176.
- 10 S. M. Lehar, T. Pillow, M. Xu, L. Staben, K. K. Kajihara, R. Vandlen, L. DePalatis, H. Raab, W. L. Hazenbos, J. Hiroshi Morisaki, J. Kim, S. Park, M. Darwish, B.-C. Lee, H. Hernandez, K. M. Loyet, P. Lupardus, R. Fong, D. Yan, C. Chalouni, E. Luis, Y. Khalfin, E. Plise, J. Cheong, J. P. Lyssikatos, M. Strandh, K. Koefoed, P. S. Andersen, J. A. Flygare, M. Wah Tan, E. J. Brown and S. Mariathasan, *Nature*, 2015, **527**, 323–328.
- 11 H. K. Kim, V. Thammavongsa, O. Schneewind and D. Missiakas, *Curr. Opin. Microbiol.*, 2012, **15**, 92–99.
- 12 S. Esposito, S. Noviello and S. Leone, *Curr. Opin. Infect. Dis.*, 2016, **29**, 109–115.
- 13 G. Gao, Y. W. Jiang, H. R. Jia and F. G. Wu, *Biomaterials*, 2019, **188**, 83–95.
- 14 C. Walsh, *Nature*, 2000, **406**, 775–781.
- 15 Z. Zhao, R. Yan, X. Yi, J. Li, J. Rao, Z. Guo, Y. Yang, W. Li, Y.-Q. Li and C. Chen, *ACS Nano*, 2017, **11**, 4428–4438.
- 16 I. M. Chiu, B. A. Heesters, N. Ghasemlou, C. A. Von Hehn, F. Zhao, J. Tran, B. Wainger, A. Strominger, S. Muralidharan, A. R. Horswill, J. B. Wardenburg, S. W. Hwang, M. C. Carroll and C. J. Woolf, *Nature*, 2013, **501**, 52–57.
- 17 A. C. Engler, N. Wiradharma, Z. Y. Ong, D. J. Coady, J. L. Hedrick and Y. Y. Yang, *Nano Today*, 2012, **7**, 201–222.
- 18 K. Kuroda and W. F. DeGrado, *J. Am. Chem. Soc.*, 2005, **127**, 4128–4129.
- 19 B. Cao, F. Xiao, D. Xing and X. Hu, *Small*, 2018, **14**, 1802008.
- 20 B. Wang, G. X. Feng, M. Seifrid, M. Wang, B. Liu and G. C. Bazan, *Angew. Chem., Int. Ed.*, 2017, **56**, 16063–16066.
- 21 E. Baeten, J. J. Haven and T. Junkers, *Polym. Chem.*, 2017, **8**, 3815–3824.
- 22 Y. Liu, S. Ding, R. Dietrich, E. Martilbauer and K. Zhu, *Angew. Chem., Int. Ed.*, 2017, **56**, 5651–5651.
- 23 Y. C. Yang, P. He, Y. X. Wang, H. T. Bai, S. Wang, J. F. Xu and X. Zhang, *Angew. Chem., Int. Ed.*, 2017, **56**, 16239–16242.
- 24 F. Xiao, B. Cao, C. Wang, X. Guo, M. Li, D. Xing and X. Hu, *ACS Nano*, 2019, **13**, 1511–1525.
- 25 X. L. Liu, M. G. Li, T. Han, B. Cao, Z. J. Qiu, Y. Y. Li, Q. Y. Li, Y. B. Hu, Z. Y. Liu, J. W. Y. Lam, X. L. Hu and B. Z. Tang, *J. Am. Chem. Soc.*, 2019, **141**, 11259–11268.
- 26 W. Tong, Y. H. Xiong, S. Duan, X. K. Ding and F. J. Xu, *Biomater. Sci.*, 2019, **7**, 1905–1918.
- 27 X. W. He, L. H. Xiong, Z. Zhao, Z. Y. Wang, L. Luo, J. W. Y. Lan, R. T. K. Kwok and B. Z. Tang, *Theranostics*, 2019, **9**, 3223–3248.
- 28 L. L. Xu, C. He, L. W. Hui, Y. T. Xie, J. M. Li, W. D. He and L. H. Yang, *ACS Appl. Mater. Interfaces*, 2015, **7**, 27602–27607.
- 29 Y. Xi, Y. Wang, J. Gao, Y. Xiao and J. Du, *ACS Nano*, 2019, **13**, 13645–13657.
- 30 Y. Ping, X. R. Hu, Q. Yao, Q. D. Hu, S. Amini, A. Miserez and G. P. Tang, *Nanoscale*, 2016, **8**, 16486–16498.
- 31 G. Fang, W. Li, X. Shen, J. M. Perez-Aguilar, Y. Chong, X. Gao, Z. Chai, C. Chen, C. Ge and R. Zhou, *Nat. Commun.*, 2018, **9**, 129.
- 32 L. Wang, X. Zhang, X. Yu, F. Gao, Z. Shen, X. Zhang, S. Ge, J. Liu, Z. Gu and C. Chen, *Adv. Mater.*, 2019, **31**, 1901965.
- 33 D. F. Hu, H. Li, B. L. Wang, Z. Ye, W. X. Lei, F. Jia, Q. Jin, K. F. Ren and J. Ji, *ACS Nano*, 2017, **11**, 9330–9339.
- 34 W. Y. Yin, J. Yu, F. T. Lv, L. Yan, L. R. Zheng, Z. J. Gu and Y. L. Zhao, *ACS Nano*, 2016, **10**, 11000–11011.
- 35 Y. Tian, J. P. Zhang, S. W. Tang, L. Zhou and W. L. Yang, *Small*, 2016, **12**, 721–726.
- 36 S. M. Sharker, J. E. Lee, S. H. Kim, J. H. Jeong, I. In, H. Lee and S. Y. Park, *Biomaterials*, 2015, **61**, 229–238.
- 37 R. Weissleder, *Nat. Biotechnol.*, 2001, **19**, 316–317.
- 38 M. C. Wu, A. R. Deokar, J. H. Liao, P. Y. Shih and Y. C. Ling, *ACS Nano*, 2013, **7**, 1281–1290.
- 39 S. H. Kim, E. B. Kang, C. J. Jeong, S. M. Sharker, I. In and S. Y. Park, *ACS Appl. Mater. Interfaces*, 2015, **7**, 15600–15606.
- 40 B. Hu, C. Berkey, T. Feliciano, X. Chen, Z. Li, C. Chen, S. Amini, M. H. Nai, Q.-L. Lei, R. Ni, J. Wang, W. R. Leow, S. Pan, Y.-Q. Li, P. Cai, A. Miserez, S. Li, C. T. Lim, Y.-L. Wu, T. W. Odom, R. H. Dauskardt and X. Chen, *Adv. Mater.*, 2020, 1907030.
- 41 J. G. Hurdle, A. J. O'Neill, I. Chopra and R. E. Lee, *Nat. Rev. Microbiol.*, 2011, **9**, 62–75.
- 42 B. R. Saunders, J. M. Saunders, J. Mrkic and E. H. Dunlop, *Phys. Chem. Chem. Phys.*, 1999, **1**, 1562–1568.

- 43 G. Shustak, M. Gadzinowski, S. Slomkowski, A. J. Domb and D. Mandler, *New J. Chem.*, 2007, **31**, 163–168.
- 44 M. Chen, X. L. Fang, S. H. Tang and N. F. Zheng, *Chem. Commun.*, 2012, **48**, 8934–8936.
- 45 J. Yang, S. D. Zhai, H. Qin, H. Yan, D. Xing and X. L. Hu, *Biomaterials*, 2018, **176**, 1–12.
- 46 E.R. Kenawy, S. D. Worley and R. Broughton, *Biomacromolecules*, 2007, **8**, 1359–1384.
- 47 J. Chen, F. Y. K. Wang, Q. M. Liu and J. Z. Du, *Chem. Commun.*, 2014, **50**, 14482–14493.
- 48 X. L. Hu, X. Q. Zhao, B. Z. He, Z. Zhao, Z. Zheng, P. F. Zhang, X. J. Shi, R. T. K. Kwok, J. W. Y. Lam, A. J. Qin and B. Z. Tang, *Research*, 2018, **2018**, 3152870.
- 49 Y. Liu, H. J. Busscher, B. Zhao, Y. Li, Z. Zhang, H. C. van der Mei, Y. Ren and L. Shi, *ACS Nano*, 2016, **10**, 4779–4789.
- 50 A. Antonoplis, X. Y. Zang, M. A. Huttner, K. K. L. Chong, Y. B. Lee, J. Y. Co, M. R. Amieva, K. A. Kline, P. A. Wender and L. Cegelski, *J. Am. Chem. Soc.*, 2018, **140**, 16140–16151.
- 51 S. M. Silverman, J. E. Moses and K. B. Sharpless, *Chem. – Eur. J.*, 2017, **23**, 79–83.
- 52 C. H. Yang, C. H. Ren, J. Zhou, J. J. Liu, Y. M. Zhang, F. Huang, D. Ding, B. Xu and J. Liu, *Angew. Chem., Int. Ed.*, 2017, **56**, 2356–2360.
- 53 S. D. Zhai, X. L. Hu, Z. Ji, H. Qin, Z. X. Wang, Y. J. Hu and D. Xing, *Nano Lett.*, 2019, **19**, 1728–1735.
- 54 X. L. Hu, G. H. Liu, Y. Li, X. R. Wang and S. Y. Liu, *J. Am. Chem. Soc.*, 2015, **137**, 362–368.
- 55 N. Zhao, B. Y. Wu, X. L. Hu and D. Xing, *Biomaterials*, 2017, **141**, 40–49.
- 56 K. M. Au, Z. H. Lu, S. J. Matcher and S. P. Armes, *Adv. Mater.*, 2011, **23**, 5792–5795.
- 57 Y. M. Li, X. L. Hu, S. D. Tian, Y. Li, G. Q. Zhang, G. Y. Zhang and S. Y. Liu, *Biomaterials*, 2014, **35**, 1618–1626.
- 58 D. K. Roper, W. Ahn and M. Hoepfner, *J. Phys. Chem. C*, 2007, **111**, 3636–3641.
- 59 D. Wang, M. M. S. Lee, W. Xu, G. Shan, X. Zheng, R. T. K. Kwok, J. W. Y. Lam, X. Hu and B. Z. Tang, *Angew. Chem.*, 2019, **131**, 5684–5688.
- 60 C. M. Hessel, V. P. Pattani, M. Rasch, M. G. Panthani, B. Koo, J. W. Tunnell and B. A. Korgel, *Nano Lett.*, 2011, **11**, 2560–2566.
- 61 P. Huang, P. F. Rong, J. Lin, W. W. Li, X. F. Yan, M. G. Zhang, L. M. Nie, G. Niu, J. Lu, W. Wang and X. Y. Chen, *J. Am. Chem. Soc.*, 2014, **136**, 8307–8313.
- 62 Q. Tian, Q. Wang, K. X. Yao, B. Teng, J. Zhang, S. Yang and Y. Han, *Small*, 2014, **10**, 1063–1068.
- 63 J. M. Xia, W. J. Wang, X. Hai, E. Shuang, Y. Shu and J. H. Wang, *Chin. Chem. Lett.*, 2019, **30**, 421–424.
- 64 Y. W. Zhu, C. Xu, N. Zhang, X. K. Ding, B. R. Yu and F. J. Xu, *Adv. Funct. Mater.*, 2018, **28**, 1706709.
- 65 Y. M. Li, H. S. Yu, Y. F. Qian, J. M. Hu and S. Y. Liu, *Adv. Mater.*, 2014, **26**, 6734–6741.